

Ultrathin Free-Standing Nanosheets of $\text{Bi}_2\text{O}_2\text{Se}$: Room Temperature Ferroelectricity in Self-Assembled Charged Layered Heterostructure

Tanmoy Ghosh,[†] Manisha Samanta,[†] Aastha Vasdev,[‡] Kapildeb Dolui,[§] Jay Ghatak,^{||} Tanmoy Das,[⊥] Goutam Sheet,^{*‡} and Kanishka Biswas^{*‡,||,#}

[†]New Chemistry Unit, Jawaharlal Nehru Centre for Advanced Scientific Research (JNCASR), Jakkur, Bangalore 560064, India

[‡]Department of Physical Sciences, Indian Institute of Science Education and Research Mohali, Sector 81, S. A. S. Nagar, Manauli 140306, India

[§]Department of Physics and Astronomy, University of Delaware, Newark, Delaware 19716-2570, United States

^{||}International Centre for Materials Science, Jawaharlal Nehru Centre for Advanced Scientific Research (JNCASR), Jakkur, Bangalore 560064, India

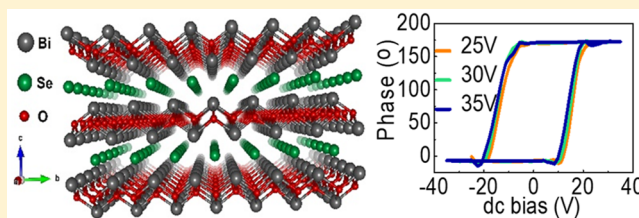
[⊥]Department of Physics, Indian Institute of Science, Bangalore 560012, India

[#]School of Advanced Materials, Jawaharlal Nehru Centre for Advanced Scientific Research (JNCASR), Jakkur, Bangalore 560064, India

Supporting Information

ABSTRACT: Ultrathin ferroelectric semiconductors with high charge carrier mobility are much coveted systems for the advancement of various electronic and optoelectronic devices. However, in traditional oxide ferroelectric insulators, the ferroelectric transition temperature decreases drastically with decreasing material thickness and ceases to exist below certain critical thickness owing to depolarizing fields. Herein, we show the emergence of an ordered ferroelectric ground state in ultrathin (~ 2 nm) single crystalline nanosheets of $\text{Bi}_2\text{O}_2\text{Se}$ at room temperature. Free-standing ferroelectric nanosheets, in which oppositely charged alternating layers are self-assembled together by electrostatic interactions, are synthesized by a simple, rapid, and scalable wet chemical procedure at room temperature. The existence of ferroelectricity in $\text{Bi}_2\text{O}_2\text{Se}$ nanosheets is confirmed by dielectric measurements and piezoresponse force spectroscopy. The spontaneous orthorhombic distortion in the ultrathin nanosheets breaks the local inversion symmetry, thereby resulting in ferroelectricity. The local structural distortion and the formation of spontaneous dipole moment were directly probed by atomic resolution scanning transmission electron microscopy and density functional theory calculations.

KEYWORDS: Bismuth oxyselenide, high-mobility semiconductor, charged layered heterostructure, two-dimensional materials, ferroelectricity, spontaneous distortion



Ultrathin two-dimensional (2D) materials play a crucial role in the future advancement of electronic, optoelectronic, energy conversion and storage, and numerous other fields with their superior properties.^{1–4} They are also known to exhibit many emerging and novel phenomena in quantum materials.^{5,6} The experimental realization of cooperative states with long-range ordering such as ferroelectricity, however, has been proved to be increasingly difficult as the materials are gradually thinned down to their monolayer limits. The realization of a ferroelectric state in the monolayer limits is not only of fundamental interest but also holds immense potential for various electronic and optoelectronic applications such as in random access memory.⁷ The ferroelectric transition temperature, however, reduces drastically in traditional three-dimensional (3D) ferroelectric insulators like PbTiO_3 , BaTiO_3 , etc. when they are gradually thinned down owing to the depolarization field^{8–12} and ferroelectricity ceases to exist below certain critical thickness.¹³ Many layered materials, on

the other hand, have been predicted to host ferroelectric states even in their monolayer limits,^{14–19} and such layered materials are also preferred in device applications for their weak interlayer interactions which minimize interfacial coupling. Room temperature ferroelectricity in ultrathin layered van der Waal (vdW) materials has been experimentally realized in CuInP_2S_6 down to 4 nm,²⁰ and so far, the only other layered materials in which ferroelectricity has been experimentally realized in the atomically thin geometry are SnTe ,²¹ In_2Se_3 ,^{22–25} and MoTe_2 ,²⁶ despite numerous theoretical predictions.

Following the sensation of graphene, many other layered 2D materials like phosphorene, transition-metal dichalcogenides

Received: June 7, 2019

Revised: July 25, 2019

Published: July 26, 2019

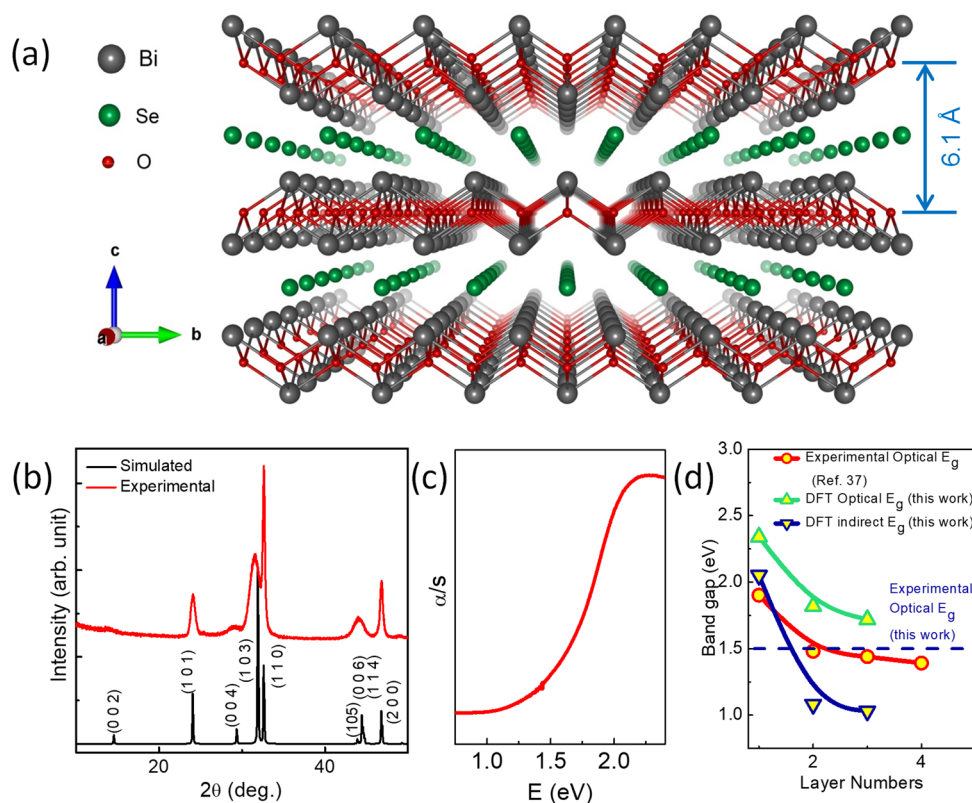


Figure 1. (a) Layered crystal structure of Bi₂O₂Se showing alternative stacks of [Bi₂O₂]²⁺ and Se²⁻ layers. (b) XRD pattern of the synthesized Bi₂O₂Se nanosheets after vacuum drying measured with Cu K α X-ray along with the simulated XRD pattern. (c) Optical absorption spectrum of Bi₂O₂Se nanosheets showing band gap of 1.5 eV. (d) Experimental and theoretical optical band gap variation with layer numbers for a Bi₂O₂Se nanosheet.

(TMDs), MXenes, etc. have been successfully synthesized in their ultrathin form.^{27–31} The discovery of new 2D materials in their ultrathin geometry is, in fact, one of the major thrust areas to mitigate the various impediments with the current candidate 2D materials. Recently, vdW heterostructures, either the assembly of different atomically thin 2D materials forming a new heterostructure^{32,33} or the synthesis of naturally occurring layered heterostructure materials in their ultrathin form,^{34,35} have gained wide attention as they offer manipulation of a wide range of functionalities. Recently, the layered oxy-chalcogenide material Bi₂O₂Se has emerged as a compelling 2D material for its extremely high carrier mobility (>20,000 cm² V⁻¹ s⁻¹ at 2 K) with very low effective mass (0.14 m₀),³⁶ and indirect size tunable band gap (bulk band gap ~0.8 eV),^{36,37} which is excellent for electronic and optoelectronic applications^{38–42} and air stability. Moreover, recent density functional theory (DFT) calculations predict that bulk Bi₂O₂Se may possess a ferroelectric state under an in-plane biaxial strain and exhibits piezoelectric response an order of magnitude higher than that of monolayer MoS₂.⁴³ Most of the ferroelectric materials, including the recently discovered layered CuInP₂S₆, are insulators with a large band gap. Therefore, it is worthwhile to stabilize a ferroelectric state in the atomically thin Bi₂O₂Se for its semiconducting nature and high charge carrier mobility. The robust surface states of Bi₂O₂Se^{38,44} against defects is also desirable in ultrathin ferroelectrics for minimizing the interfacial effects.⁴⁵

Herein, we demonstrate a simple, rapid, and scalable synthesis of ultrathin single crystalline Bi₂O₂Se nanosheets by solution-based self-assembly of oppositely charged layers at

room temperature. Atomic force microscopy (AFM) reveals that the obtained nanosheets are ~2 nm thick with a smooth surface. Field emission scanning electron microscopy (FESEM) and scanning transmission electron microscopy (STEM) images confirm that the synthesized nanosheets have lateral dimension in the range of 100–200 nm. The measurement of temperature-dependent dielectric constant reveals that the ferroelectric transition occurs at ~235 °C. The piezoresponse force microscopy (PFM) further confirms the presence of spontaneous polarization and 180° polarization switching under an external field at room temperature. To understand the origin of ferroelectricity in ultrathin Bi₂O₂Se nanosheets, we have carried out atomic resolution STEM and corroborated the results with DFT calculations. We found that these free-standing nanosheets have spontaneous orthorhombic distortion which breaks the inversion symmetry locally in the tetragonal crystal structure. Thus, dipole moments develop spontaneously and becomes aligned ferroelectrically.

Bi₂O₂Se, with the absence of a well-defined vdW gap, however, intrinsically distinguishes itself from the family of vdW solids. The tetragonal structure (*I4/mmm* space group, *a* = 3.88 Å, *c* = 12.16 Å) of Bi₂O₂Se is formed by the alternate stacking of positively charged [Bi₂O₂]²⁺ and negatively charged Se²⁻ layers along the crystallographic *c*-direction (Figure 1a).^{36,46} Although Bi₂O₂Se has a layered crystal structure, the interlayer interaction is of electrostatic type which arises out of positively charged [Bi₂O₂]²⁺ and negatively charged Se²⁻ stacking layers and is stronger than vdW interaction.³⁶

A pivotal part of the success of any 2D material in practical applications is the development of a rapid, scalable, and simple

synthesis process. Various methods of preparation have been developed for the established candidate 2D materials like graphene and TMDCs, which often exploit the weak nature of the interlayer vdW force.^{27–30} The strong interlayer electrostatic force in Bi₂O₂Se, however, renders such traditional top-down synthesis processes, like exfoliation of producing atomically thin vdW materials, unfeasible here. The bottom-up approaches also face considerable challenges as the topmost layer always attracts the oppositely charged next layer and results in vertical growth. So far, ultrathin Bi₂O₂Se nanosheets were grown using chemical vapor deposition (CVD) mostly on freshly cleaved fluorophlogopite mica^{36–38,41} where the electrostatic interaction between the substrate and epitaxial nanosheet layer facilitate the lateral growth. Recently, Tan et al. has also been successful in growing wafer-scale single crystalline Bi₂O₂Se films on lattice matched perovskite oxide substrates such as SrTiO₃, LaAlO₃, and their derivatives using CVD.⁴⁷ However, atomically thin nanosheets were obtained only in few cases so far.^{36,37,47} Furthermore, the realization of ferroelectricity requires careful selection of a lattice matched substrate to minimize misfit strain⁴⁸ and interfacial coupling.⁴⁵ The use of charged substrate-like fluorophlogopite mica^{36–38,41} or chemical etching used for substrate transfer⁴¹ can have severe effects on the ferroelectric state.

Here, we have synthesized free-standing, single crystalline nanosheets of Bi₂O₂Se in a simple solution-based method by the reaction of bismuth nitrate (Bi(NO₃)₃) and selenourea (SeC(NH₂)₂) in an alkaline medium at room temperature (see details in Methods, Supporting Information). This is a one-pot synthesis method which can be carried out in a glass beaker in ambient conditions. The reaction process is also very fast in which pure and ultrathin nanosheets with high crystalline quality grow within 10 min. The reaction is easily scalable up to ~1 g in laboratory conditions. In aqueous medium, Bi(NO₃)₃ undergoes hydrolysis to produce BiONO₃, and this hydrolysis process further expedites in the alkaline medium after the addition of NaOH and KOH. In alkaline medium, SeC(NH₂)₂ also decomposes and produces selenide ions (Se²⁻). These Se²⁻ ions then interact with BiONO₃ to produce Bi₂O₂Se which precipitates as a dark brown color product. Thus, positively charged [Bi₂O₂]²⁺ and negatively charged Se²⁻ layers generated from two different precursors in alkaline medium self-assembled electrostatically to form ultrathin Bi₂O₂Se nanosheets.

The room temperature powder X-ray diffraction (XRD) pattern of the as-synthesized nanosheets shows only a broad hump (Figure S1) which indicates the ultrathin nature of the synthesized nanosheets. After vacuum drying the nanosheets, the XRD pattern (Figure 1b) could be indexed with the pristine Bi₂O₂Se tetragonal structure (space group *I4/mmm*). The agglomeration of the nanosheets during vacuum drying results in such a clear depiction of the XRD pattern. Energy dispersive X-ray spectroscopy (EDX) (Table S1) and inductively coupled plasma atomic emission spectroscopy (ICP-AES) (Table S2) confirm that elemental composition of the nanosheets is close to the nominal composition. EDX elemental color mapping (Figure S2) during STEM exhibits a homogeneous distribution of the elements Bi, O, and Se in the nanosheets. X-ray photoelectron spectroscopy (XPS) (Figure S3) further confirms the expected Bi(III), O(II), and Se(II) oxidation states of the elements. The morphological studies using FESEM, AFM, and transmission electron microscopy (TEM) corroborate the nanosheets ultrathin nature. FESEM

(Figure S4), STEM (Figure 2a), and low-magnification TEM micrographs (Figure 2b) clearly demonstrate the ultrathin

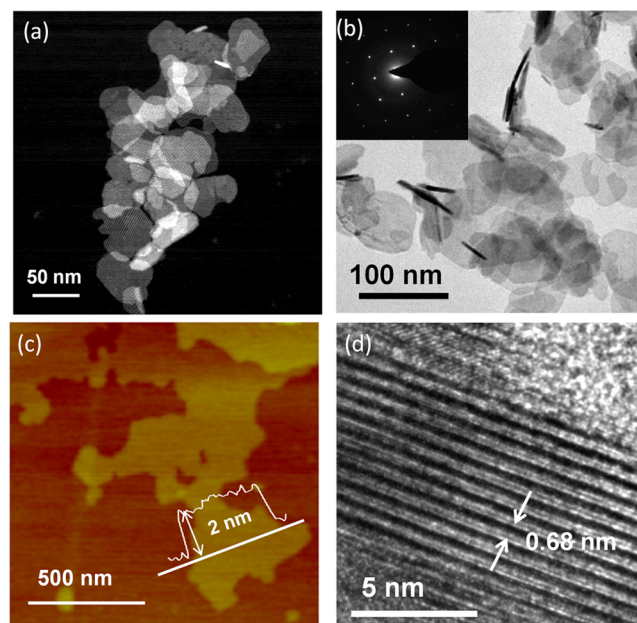


Figure 2. (a) STEM-HAADF image of Bi₂O₂Se nanosheets. (b) High-magnification TEM image of Bi₂O₂Se nanosheets. Inset shows the SAED pattern demonstrating the single crystalline nature of the nanosheet. (c) AFM image and the height profile showing Bi₂O₂Se nanosheets of 2 nm thickness, which corresponds to approximately 3 layers. (d) HRTEM image of Bi₂O₂Se nanosheet showing the layer-by-layer arrangement with separation of 0.68 Å.

morphology of the nanosheets with lateral dimensions of the individual nanosheets ranges in between 100 and 200 nm. AFM images (Figure 2c and Figure S8) reveal the thickness of most of the individual nanosheets is ~2 nm, which consists of 2–3 heterostructure layers. Furthermore, selected area electron diffraction (SAED) pattern (Figure 2b, Inset) indicates the single crystalline nature of the as-synthesized nanosheets. The layered arrangement along the crystallographic *c*-axis with a spacing of ~0.68 nm is clearly seen from the high-resolution TEM (HRTEM) image (Figure 2d). The slightly higher spacing of 0.68 nm between two [Bi₂O₂]²⁺ layers compared to the expected value of 0.61 nm from its bulk counterpart might be because of structural relaxation in these free-standing thin nanosheets. Similar structural relaxation was observed earlier also in chemical vapor deposition (CVD) grown Bi₂O₂Se nanosheets.³⁷ Theoretical analysis of Γ point phonon modes of Bi₂O₂Se yields four Raman active modes: A_{1g} and B_{1g} modes corresponding to the out of plane vibration of Bi and O atoms, respectively, and E_g¹ and E_g² modes corresponding to the in-plane vibration of Bi and O atoms, respectively.^{49–51} Previous studies indicate that out of these four Raman active modes, only the A_{1g} mode is observable in the backscattering configuration.^{37,49,50} Figure S5 exhibits the room temperature Raman spectra of the Bi₂O₂Se nanosheets in which the A_{1g} mode is evident around ~151.9 cm⁻¹. A comparison between the Raman spectra of bulk and nanosheet Bi₂O₂Se samples indicates a low-energy shift of the A_{1g} mode in the nanosheet (Figure S5) due to phonon softening, corresponding to weakened interlayer coupling in the ultrathin nanosheets.⁴⁹

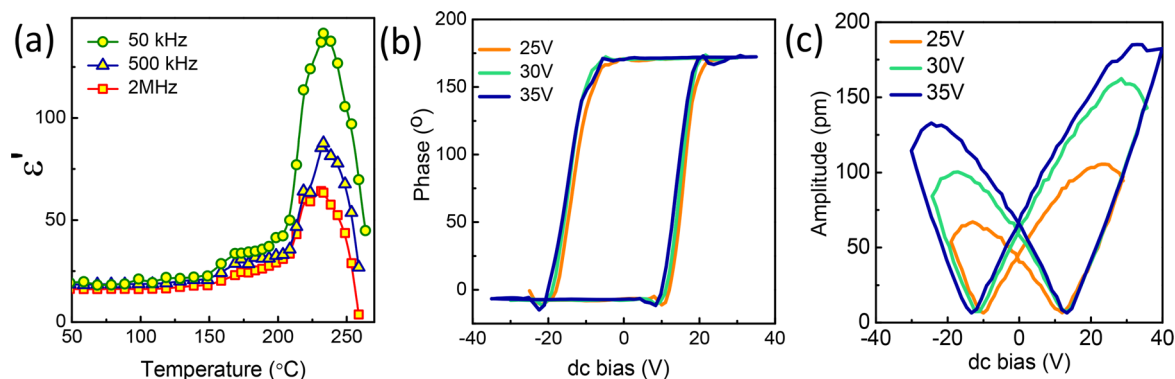


Figure 3. (a) Temperature variation of the real part of relative permittivity (ϵ') at different frequencies for $\text{Bi}_2\text{O}_2\text{Se}$ nanosheet. “Off-state” (b) phase and (c) amplitude of SS-PFM signal from $\text{Bi}_2\text{O}_2\text{Se}$ nanosheet at room temperature exhibiting ferroelectricity with 180° polarization switching.

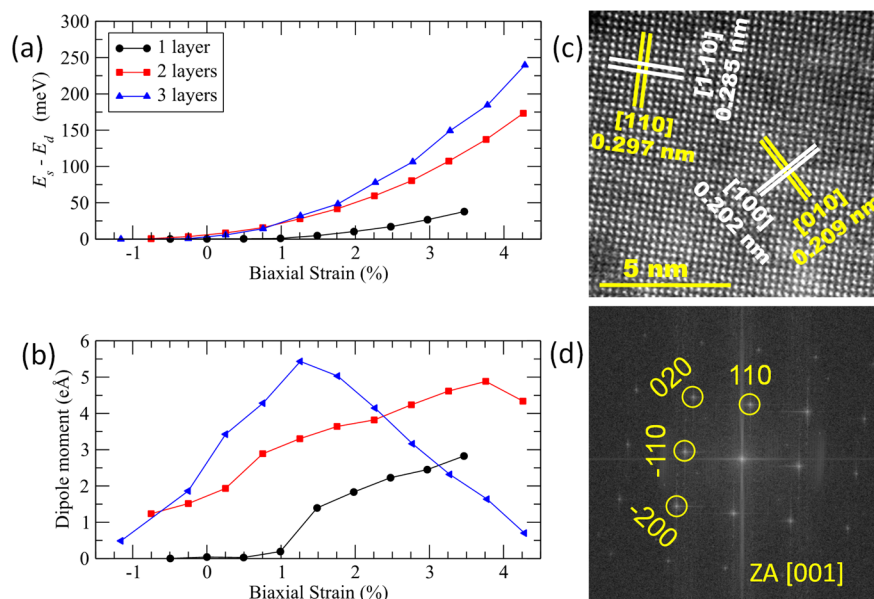


Figure 4. (a) Variation of $\Delta E = E_s - E_d$ and (b) total dipole moment under strain for monolayer, bilayer, and trilayer $\text{Bi}_2\text{O}_2\text{Se}$ nanosheets. E_s and E_d denote the total energy for symmetrical and distorted structures, respectively. (c) Atomic resolution HAADF-STEM image projected along the $[001]$ direction exhibiting deviation between interatomic distances along $[110]$ and $[1-10]$ directions and along $[100]$ and $[010]$ directions. (d) Fast Fourier transformation (FFT) of the atomic resolution STEM image shown in (c).

The optical band gap of the as-synthesized nanosheets measured using diffuse reflectance spectroscopy was found to be ~ 1.5 eV (Figure 1c). The previous report³⁷ on CVD grown nanosheets indicated for the thickness tunability of band gap, where optical band gap increases with decreasing layer thickness due to the quantum confinement effect. Our DFT calculations (Figure 1d and Figure S6) also indicate a similar enhancement in optical band gap at the Γ point due to quantum confinements, as the thickness decreases with a maximum optical band gap of 2.34 eV for the monolayer nanosheet. The comparison of experimentally obtained optical band gap for our solution synthesized nanosheets (dashed line in Figure 1d) with the reported optical band gap of CVD grown nanosheets further indicates that the synthesized nanosheets are only $\sim 2-3$ layers thick. Additionally, an indirect band gap also exists between the Γ and X points. While Se-p orbital mainly contributes to the valence band maxima at X point, the conduction band minima at the Γ point originates from the Bi-p orbital, resulting in an indirect band gap along the $\Gamma-X$ direction (Figure S6). Although the band topology does not change from the monolayer to the bulk, the

dispersion of the valence band decreases with the decrease in thickness with a corresponding increase in their effective mass (Figure S6).

The temperature-dependent dielectric property of the nanosheets at different frequencies is shown in Figure 3a. The temperature variation of relative permittivity, $\epsilon'(T)$, shows a clear maximum at $T_c \sim 235$ $^{\circ}\text{C}$ without any observable frequency dependence, elucidating a ferroelectric-like transition (Figure 3a). ϵ' decreases as frequency increases with the maximum values of ϵ' of 64.2, 87.7, and 141.5 at frequencies 2 MHz, 500 kHz, and 50 kHz, respectively. The differential scanning calorimetric (DSC) signal of $\text{Bi}_2\text{O}_2\text{Se}$ nanosheets also shows a transition around the same temperature region where we observed ferroelectric transition in the temperature variation of ϵ' (Figure S7).

To further ascertain the ferroelectric state, we carried out switching spectroscopy by piezoresponse force microscopy (PFM)^{52,53} to show the existence of a spontaneous polarization state and its switching behavior under an externally applied electric field. Figure 3b,c exhibits the observed hysteresis behavior in the “off-state” piezoresponse signal at room

temperature. The phase of the PFM response signal is correlated with the domain's polarization direction, and for a ferroelectric sample, the electrical polarization, and thus the phase of the PFM response signal, should show hysteresis behavior with 180° polarization switching. Figure 3b clearly exhibits the hysteresis behavior with a sharp 180° switching of electrical polarization at different applied dc bias (V_{dc}). The coercive field is ~ 14 V, which is large, indicating a strong energy barrier between the two opposite polarization states. The amplitude of the PFM response signal is related to the magnitude of the local electromechanical response experienced by the PFM cantilever and exhibits hysteresis behavior with an expected butterfly-shaped hysteresis loop (Figure 3c).

The appearance of room temperature ferroelectricity in ultrathin $\text{Bi}_2\text{O}_2\text{Se}$ nanosheets is rather surprising, considering its known centrosymmetric crystal structure in the bulk phase. Therefore, to further understand the origin of the observed ferroelectric behavior in the nanosheets, we performed DFT calculations for a symmetric structure as well as distorted structure in which Bi and O/Se atoms were displaced diagonally from their equilibrium positions in opposite directions. To investigate the effect of strain in the appearance of ferroelectricity, we have carried out further simulations onto the system by applying both compressive and tensile planar biaxial strains. The strain magnitude has been quantified as $\zeta = (a - a_0)/a_0$, where a and a_0 are the in-plane lattice constants for the strained and pristine nanosheets, respectively. Figure 4a,b shows the energetics between symmetric and distorted structures and dipole moments, respectively, at different biaxial strains applied in various nanosheets, in which thicknesses range from monolayer to trilayer. Likewise the ferroelectricity in bulk $\text{Bi}_2\text{O}_2\text{Se}$ predicted previously by theoretical calculations,⁴³ our calculations show that the ferroelectricity persists in the monolayer nanosheet only for $\zeta > 1\%$ (Figure 4b). In the ferroelectric phase, the structural inversion symmetry gets broken by atomic displacement of Bi and O atoms. In bulk $\text{Bi}_2\text{O}_2\text{Se}$, the $[\text{Bi}_2\text{O}_2]^{2+}$ layer is made by $(\text{BiO})_2$ rhombic network. The atomic displacement of Bi and O atoms distorts this rhombic network in the nanosheet. Interestingly, we find that both the distorted bilayer and trilayer nanosheets exhibit spontaneous dipole moments even in the unstrained phase, unlike the bulk and monolayer cases where certain strains are required to induce the ferroelectricity. For bilayer and trilayer nanosheets, the dipole moments increase initially with tensile strain and subsequently reach a maximum value at 1.2% and 3.8% strain, respectively, producing a dome shape behavior (Figure 4b). For the compressive strain, the dipole moment decreases monotonically and seems to vanish by $\zeta \sim 1.5\%$ in the few-layer cases. At various ζ values, we compare the energy difference $\Delta E = E_s - E_d$, where E_s and E_d are the total energies for the symmetric and distorted structures. We find that ΔE remains nearly zero for monolayer nanosheets for both compressive and tensile strains up to 1%, which indicates that such spontaneous structural distortion is an energetically possible scenario (Figure 4a). Furthermore, our results indicate that structural distortion is energetically more favorable for compressive strains than for tensile strains. In the case of tensile strain, we find that structural distortions gradually cost more energy as the strain magnitude ζ or the nanosheet thickness increases (Figure 4a).

To experimentally verify the presence of spontaneous distortion in the nanosheets, we carried out atomic resolution high-angle annular dark-field (HAADF)-STEM imaging of the

$\text{Bi}_2\text{O}_2\text{Se}$ nanosheets (Figure 4c). The tetragonal $I4/mmm$ symmetry demands the interplanar spacing d_{h00} for the $(h00)$ and d_{0k0} for the $(0k0)$ family of lattice planes to be identical. However, from the electron diffraction pattern (Figure 4d) obtained by FFT of the atomic resolution STEM images, we found that d_{200} and d_{020} are non-equivalent by ~ 0.11 Å. Correspondingly, in real space, from the atomic resolution STEM images, we find that deviation between interatomic distances along $[110]$ and $[1-10]$ directions is ~ 0.12 Å. This indicates the presence of diagonal distortion in the $\text{Bi}_2\text{O}_2\text{Se}$ nanosheets. The interatomic distances along the $[100]$ and $[010]$ directions are also unequal by ~ 0.07 Å, which means that lattice parameters a and b are no longer equal. The distorted scenario is well supported by the DFT calculations which predict the distortion of the Bi–O bond length is about 0.05 Å along $[100]$ and $[010]$ directions for bilayer and trilayer nanosheets under zero strain. The presence of these spontaneous distortions thus changes the system from tetragonal (D_{4h}) (which is the symmetry for the bulk phase) to an orthorhombic (C_{2v}) nanosheet system along with a local inversion symmetry breaking, which supports the presence of room temperature ferroelectricity in the free-standing ultrathin $\text{Bi}_2\text{O}_2\text{Se}$ nanosheets.

In summary, we demonstrated a simple and scalable solution-based synthesis to prepare self-assembled charged layered heterostructure nanosheets of $\text{Bi}_2\text{O}_2\text{Se}$. The obtained nanosheets are ultrathin (~ 2 nm), single crystalline, and free-standing in nature. We found that an intriguing ferroelectric order emerges, which is stable even at room temperature, due to spontaneous orthorhombic distortion in the nanosheets. The distortion is created by atomic displacement of Bi and O atoms which breaks the local inversion symmetry and facilitates the formation of spontaneous dipole moments. The development of room temperature ferroelectricity in the semiconducting nanosheets of this high-mobility $\text{Bi}_2\text{O}_2\text{Se}$ semiconductor is an important advancement for the electronic and optoelectronic devices.

■ ASSOCIATED CONTENT

Supporting Information

The Supporting Information is available free of charge on the ACS Publications website at DOI: 10.1021/acs.nanolett.9b02312.

Details of synthesis, experimental, and theoretical methods, and tables of elemental compositions; additional XRD, FESEM, XPS, TEM, Raman spectra, band structure, DSC, and AFM (PDF)

■ AUTHOR INFORMATION

Corresponding Authors

*E-mail: kanishka@jncasr.ac.in.

*E-mail: goutam@iisermohali.ac.in.

ORCID

Kanishka Biswas: 0000-0001-9119-2455

Author Contributions

K.B. designed the problem. T.G., M.S., and K.B. carried out the synthesis and characterization of the sample and conducted the dielectric measurements. A.V. and G.S. performed the PFM measurements. J.G. contributed to the STEM imaging. K.D. and T.D. performed the theoretical calculations. All authors were involved in writing the manuscript.

Notes

The authors declare no competing financial interest.

ACKNOWLEDGMENTS

This work was partially supported by the Nanomission, DST, and Sheikh Saqr Laboratory, JNCASR. M.S. thanks the UGC for research fellowship.

REFERENCES

- (1) Akinwande, D.; Petrone, N.; Hone, J. Two-dimensional flexible nanoelectronics. *Nat. Commun.* **2014**, *5*, 5678.
- (2) Wang, Q. H.; Kalantar-Zadeh, K.; Kis, A.; Coleman, J. N.; Strano, M. S. Electronics and optoelectronics of two-dimensional transition metal dichalcogenides. *Nat. Nanotechnol.* **2012**, *7*, 699–712.
- (3) Deng, D.; Novoselov, K. S.; Fu, Q.; Zheng, N.; Tian, Z.; Bao, X. Catalysis with two-dimensional materials and their heterostructures. *Nat. Nanotechnol.* **2016**, *11*, 218–230.
- (4) Bonaccorso, F.; Colombo, L.; Yu, G.; Stoller, M.; Tozzini, V.; Ferrari, A. C.; Ruoff, R. S.; Pellegrini, V. Graphene, related two-dimensional crystals, and hybrid systems for energy conversion and storage. *Science* **2015**, *347*, 1246501.
- (5) Xu, X.; Yao, W.; Xiao, D.; Heinz, T. F. Spin and pseudospins in layered transition metal dichalcogenides. *Nat. Phys.* **2014**, *10*, 343–350.
- (6) Basov, D. N.; Averitt, R. D.; Hsieh, D. Towards properties on demand in quantum materials. *Nat. Mater.* **2017**, *16*, 1077–1088.
- (7) Garcia, V.; Bibes, M. Ferroelectric tunnel junctions for information storage and processing. *Nat. Commun.* **2014**, *5*, 4289.
- (8) Fong, D. D.; Stephenson, G. B.; Streiffer, S. K.; Eastman, J. A.; Auciello, O.; Fuoss, P. H.; Thompson, C. Ferroelectricity in ultrathin perovskite films. *Science* **2004**, *304*, 1650.
- (9) Fong, D. D.; Kolpak, A. M.; Eastman, J. A.; Streiffer, S. K.; Fuoss, P. H.; Stephenson, G. B.; Thompson, C.; Kim, D. M.; Choi, K. J.; Eom, C. B.; Grinberg, I.; Rappe, A. M. Stabilization of Monodomain Polarization in Ultrathin PbTiO₃ Films. *Phys. Rev. Lett.* **2006**, *96*, 127601.
- (10) Kornev, I.; Fu, H.; Bellaiche, L. Ultrathin Films of Ferroelectric Solid Solutions under a Residual Depolarizing Field. *Phys. Rev. Lett.* **2004**, *93*, 196104.
- (11) Tenne, D. A.; Turner, P.; Schmidt, J. D.; Biegalski, M.; Li, Y. L.; Chen, L. Q.; Soukiassian, A.; Trolier-McKinstry, S.; Schlom, D. G.; Xi, X. X.; Fong, D. D.; Fuoss, P. H.; Eastman, J. A.; Stephenson, G. B.; Thompson, C.; Streiffer, S. K. Ferroelectricity in Ultrathin BaTiO₃ Films: Probing the Size Effect by Ultraviolet Raman Spectroscopy. *Phys. Rev. Lett.* **2009**, *103*, 177601.
- (12) Dawber, M.; Rabe, K. M.; Scott, J. F. Physics of thin-film ferroelectric oxides. *Rev. Mod. Phys.* **2005**, *77*, 1083–1130.
- (13) Junquera, J.; Ghosez, P. Critical thickness for ferroelectricity in perovskite ultrathin films. *Nature* **2003**, *422*, 506–509.
- (14) Vasudevan, R. K.; Balke, N.; Maksymovych, P.; Jesse, S.; Kalinin, S. V. Ferroelectric or non-ferroelectric: Why so many materials exhibit “ferroelectricity” on the nanoscale. *Appl. Phys. Rev.* **2017**, *4*, 021302.
- (15) Cui, C.; Xue, F.; Hu, W.-J.; Li, L.-J. Two-dimensional materials with piezoelectric and ferroelectric functionalities. *npj 2D Mater. Appl.* **2018**, *2*, 18.
- (16) Wu, M.; Jena, P. The rise of two-dimensional van der Waals ferroelectrics. *Wiley Interdiscip. Rev. Comput. Mol. Sci.* **2018**, *8*, No. e1365.
- (17) Shirodkar, S. N.; Waghmare, U. V. Emergence of Ferroelectricity at a Metal-Semiconductor Transition in a 1T Monolayer of MoS₂. *Phys. Rev. Lett.* **2014**, *112*, 157601.
- (18) Fei, R.; Kang, W.; Yang, L. Ferroelectricity and Phase Transitions in Monolayer Group-IV Monochalcogenides. *Phys. Rev. Lett.* **2016**, *117*, 097601.
- (19) Guan, S.; Liu, C.; Lu, Y.; Yao, Y.; Yang, S. A. Tunable ferroelectricity and anisotropic electric transport in monolayer β-GeSe. *Phys. Rev. B: Condens. Matter Mater. Phys.* **2018**, *97*, 144104.
- (20) Liu, F.; You, L.; Seyler, K. L.; Li, X.; Yu, P.; Lin, J.; Wang, X.; Zhou, J.; Wang, H.; He, H.; Pantelides, S. T.; Zhou, W.; Sharma, P.; Xu, X.; Ajayan, P. M.; Wang, J.; Liu, Z. Room-temperature ferroelectricity in CuInP₂S₆ ultrathin flakes. *Nat. Commun.* **2016**, *7*, 12357.
- (21) Chang, K.; Liu, J.; Lin, H.; Wang, N.; Zhao, K.; Zhang, A.; Jin, F.; Zhong, Y.; Hu, X.; Duan, W.; Zhang, Q.; Fu, L.; Xue, Q.-K.; Chen, X.; Ji, S.-H. Discovery of robust in-plane ferroelectricity in atomically thick SnTe. *Science* **2016**, *353*, 274.
- (22) Xiao, J.; Zhu, H.; Wang, Y.; Feng, W.; Hu, Y.; Dasgupta, A.; Han, Y.; Wang, Y.; Muller, D. A.; Martin, L. W.; Hu, P.; Zhang, X. Intrinsic Two-Dimensional Ferroelectricity with Dipole Locking. *Phys. Rev. Lett.* **2018**, *120*, 227601.
- (23) Zhou, Y.; Wu, D.; Zhu, Y.; Cho, Y.; He, Q.; Yang, X.; Herrera, K.; Chu, Z.; Han, Y.; Downer, M. C.; Peng, H.; Lai, K. Out-of-Plane Piezoelectricity and Ferroelectricity in Layered α-In₂Se₃ Nanoflakes. *Nano Lett.* **2017**, *17*, 5508–5513.
- (24) Cui, C.; Hu, W.-J.; Yan, X.; Addiego, C.; Gao, W.; Wang, Y.; Wang, Z.; Li, L.; Cheng, Y.; Li, P.; Zhang, X.; Alshareef, H. N.; Wu, T.; Zhu, W.; Pan, X.; Li, L.-J. Intercorrelated In-Plane and Out-of-Plane Ferroelectricity in Ultrathin Two-Dimensional Layered Semiconductor In₂Se₃. *Nano Lett.* **2018**, *18*, 1253–1258.
- (25) Zheng, C.; Yu, L.; Zhu, L.; Collins, J. L.; Kim, D.; Lou, Y.; Xu, C.; Li, M.; Wei, Z.; Zhang, Y.; Edmonds, M. T.; Li, S.; Seidel, J.; Zhu, Y.; Liu, J. Z.; Tang, W.-X.; Fuhrer, M. S. Room temperature in-plane ferroelectricity in van der Waals In₂Se₃. *Sci. Adv.* **2018**, *4*, eaar7720.
- (26) Yuan, S.; Luo, X.; Chan, H. L.; Xiao, C.; Dai, Y.; Xie, M.; Hao, J. Room-temperature ferroelectricity in MoTe₂ down to the atomic monolayer limit. *Nat. Commun.* **2019**, *10*, 1775.
- (27) Anasori, B.; Lukatskaya, M. R.; Gogotsi, Y. 2D metal carbides and nitrides (MXenes) for energy storage. *Nat. Rev. Mater.* **2017**, *2*, 16098.
- (28) Chhowalla, M.; Shin, H. S.; Eda, G.; Li, L.-J.; Loh, K. P.; Zhang, H. The chemistry of two-dimensional layered transition metal dichalcogenide nanosheets. *Nat. Chem.* **2013**, *5*, 263–275.
- (29) Nicolosi, V.; Chhowalla, M.; Kanatzidis, M. G.; Strano, M. S.; Coleman, J. N. Liquid Exfoliation of Layered Materials. *Science* **2013**, *340*, 1226419.
- (30) Mannix, A. J.; Kiraly, B.; Hersam, M. C.; Guisinger, N. P. Synthesis and chemistry of elemental 2D materials. *Nat. Rev. Chem.* **2017**, *1*, 0014.
- (31) Tan, C.; Cao, X.; Wu, X.-J.; He, Q.; Yang, J.; Zhang, X.; Chen, J.; Zhao, W.; Han, S.; Nam, G.-H.; Sindoro, M.; Zhang, H. Recent Advances in Ultrathin Two-Dimensional Nanomaterials. *Chem. Rev.* **2017**, *117*, 6225–6331.
- (32) Geim, A. K.; Grigorieva, I. V. Van der Waals heterostructures. *Nature* **2013**, *499*, 419–425.
- (33) Novoselov, K. S.; Mishchenko, A.; Carvalho, A.; Castro Neto, A. H. 2D materials and van der Waals heterostructures. *Science* **2016**, *353*, aac9439.
- (34) Chatterjee, A.; Biswas, K. Solution-Based Synthesis of Layered Intergrowth Compounds of the Homologous Pb_mBi_{2n}Te_{3n+m} Series as Nanosheets. *Angew. Chem., Int. Ed.* **2015**, *54*, 5623–5627.
- (35) Banik, A.; Biswas, K. Synthetic Nanosheets of Natural van der Waals Heterostructures. *Angew. Chem.* **2017**, *129*, 14753–14758.
- (36) Wu, J.; Yuan, H.; Meng, M.; Chen, C.; Sun, Y.; Chen, Z.; Dang, W.; Tan, C.; Liu, Y.; Yin, J.; Zhou, Y.; Huang, S.; Xu, H. Q.; Cui, Y.; Hwang, H. Y.; Liu, Z.; Chen, Y.; Yan, B.; Peng, H. High electron mobility and quantum oscillations in non-encapsulated ultrathin semiconducting Bi₂O₂Se. *Nat. Nanotechnol.* **2017**, *12*, 530–534.
- (37) Wu, J.; Tan, C.; Tan, Z.; Liu, Y.; Yin, J.; Dang, W.; Wang, M.; Peng, H. Controlled Synthesis of High-Mobility Atomically Thin Bismuth Oxyselenide Crystals. *Nano Lett.* **2017**, *17*, 3021–3026.
- (38) Li, J.; Wang, Z.; Wen, Y.; Chu, J.; Yin, L.; Cheng, R.; Lei, L.; He, P.; Jiang, C.; Feng, L.; He, J. High-Performance Near-Infrared Photodetector Based on Ultrathin Bi₂O₂Se Nanosheets. *Adv. Funct. Mater.* **2018**, *28*, 1706437.
- (39) Yin, J.; Tan, Z.; Hong, H.; Wu, J.; Yuan, H.; Liu, Y.; Chen, C.; Tan, C.; Yao, F.; Li, T.; Chen, Y.; Liu, Z.; Liu, K.; Peng, H. Ultrafast

and highly sensitive infrared photodetectors based on two-dimensional oxyselenide crystals. *Nat. Commun.* **2018**, *9*, 3311.

(40) Tian, X.; Luo, H.; Wei, R.; Zhu, C.; Guo, Q.; Yang, D.; Wang, F.; Li, J.; Qiu, J. An Ultrabroadband Mid-Infrared Pulsed Optical Switch Employing Solution-Processed Bismuth Oxyselenide. *Adv. Mater.* **2018**, *30*, 1801021.

(41) Fu, Q.; Zhu, C.; Zhao, X.; Wang, X.; Chaturvedi, A.; Zhu, C.; Wang, X.; Zeng, Q.; Zhou, J.; Liu, F.; Tay, B. K.; Zhang, H.; Pennycook, S. J.; Liu, Z. Ultrasensitive 2D Bi₂O₂Se Phototransistors on Silicon Substrates. *Adv. Mater.* **2019**, *31*, 1804945.

(42) Wu, J.; Liu, Y.; Tan, Z.; Tan, C.; Yin, J.; Li, T.; Tu, T.; Peng, H. Chemical Patterning of High-Mobility Semiconducting 2D Bi₂O₂Se Crystals for Integrated Optoelectronic Devices. *Adv. Mater.* **2017**, *29*, 1704060.

(43) Wu, M.; Zeng, X. C. Bismuth Oxychalcogenides: A New Class of Ferroelectric/Ferroelastic Materials with Ultra High Mobility. *Nano Lett.* **2017**, *17*, 6309–6314.

(44) Chen, C.; Wang, M.; Wu, J.; Fu, H.; Yang, H.; Tian, Z.; Tu, T.; Peng, H.; Sun, Y.; Xu, X.; Jiang, J.; Schröter, N. B. M.; Li, Y.; Pei, D.; Liu, S.; Ekahana, S. A.; Yuan, H.; Xue, J.; Li, G.; Jia, J.; Liu, Z.; Yan, B.; Peng, H.; Chen, Y. Electronic structures and unusually robust bandgap in an ultrahigh-mobility layered oxide semiconductor, Bi₂O₂Se. *Sci. Adv.* **2018**, *4*, No. eaat8355.

(45) Zubko, P.; Gariglio, S.; Gabay, M.; Ghosez, P.; Triscone, J.-M. Interface Physics in Complex Oxide Heterostructures. *Annu. Rev. Condens. Matter Phys.* **2011**, *2*, 141–165.

(46) Ruleova, P.; Drasar, C.; Lostak, P.; Li, C.-P.; Ballikaya, S.; Uher, C. Thermoelectric properties of Bi₂O₂Se. *Mater. Chem. Phys.* **2010**, *119*, 299–302.

(47) Tan, C.; Tang, M.; Wu, J.; Liu, Y.; Li, T.; Liang, Y.; Deng, B.; Tan, Z.; Tu, T.; Zhang, Y.; Liu, C.; Chen, J.-H.; Wang, Y.; Peng, H. Wafer-Scale Growth of Single-Crystal 2D Semiconductor on Perovskite Oxides for High-Performance Transistors. *Nano Lett.* **2019**, *19*, 2148–2153.

(48) Schlom, D. G.; Chen, L.-Q.; Eom, C.-B.; Rabe, K. M.; Streiffer, S. K.; Triscone, J.-M. Strain Tuning of Ferroelectric Thin Films. *Annu. Rev. Mater. Res.* **2007**, *37*, 589–626.

(49) Cheng, T.; Tan, C.; Zhang, S.; Tu, T.; Peng, H.; Liu, Z. Raman Spectra and Strain Effects in Bismuth Oxychalcogenides. *J. Phys. Chem. C* **2018**, *122*, 19970–19980.

(50) Pereira, A. L. J.; Santamaría-Pérez, D.; Ruiz-Fuertes, J.; Manjón, F. J.; Cuenca-Gotor, V. P.; Vilaplana, R.; Gomis, O.; Popescu, C.; Muñoz, A.; Rodríguez-Hernández, P.; Segura, A.; Gracia, L.; Beltrán, A.; Ruleova, P.; Drasar, C.; Sans, J. A. Experimental and Theoretical Study of Bi₂O₂Se Under Compression. *J. Phys. Chem. C* **2018**, *122*, 8853–8867.

(51) Xu, Y.-D.; Wang, C.; Lv, Y.-Y.; Chen, Y. B.; Yao, S.-H.; Zhou, J. Infrared and Raman spectra of Bi₂O₂X and Bi₂OX₂ (X = S, Se, and Te) studied from first principles calculations. *RSC Adv.* **2019**, *9*, 18042–18049.

(52) Jesse, S.; Baddorf, A. P.; Kalinin, S. V. Switching spectroscopy piezoresponse force microscopy of ferroelectric materials. *Appl. Phys. Lett.* **2006**, *88*, 062908.

(53) Jesse, S.; Mirman, B.; Kalinin, S. V. Resonance enhancement in piezoresponse force microscopy: Mapping electromechanical activity, contact stiffness, and Q factor. *Appl. Phys. Lett.* **2006**, *89*, 022906.

Supporting Information

Ultrathin Free-standing Nanosheets of Bi₂O₂Se: Room Temperature Ferroelectricity in Self-assembled Charged Layered Heterostructure

Tanmoy Ghosh,[†] Manisha Samanta,[†] Aastha Vasdev,[‡] Kapildeb Dolui,[§] Jay Ghatak^{||}, Tanmoy Das,[⊥] Goutam Sheet,^{‡,*} and Kanishka Biswas^{†,||,#,*}

[†]*New Chemistry Unit, Jawaharlal Nehru Centre for Advanced Scientific Research (JNCASR), Jakkur P.O., Bangalore 560064, India*

[‡]*Department of Physical Sciences, Indian Institute of Science Education and Research Mohali, Sector 81, S. A. S. Nagar, Manauli, P.O. Box 140306, India*

[§]*Department of Physics and Astronomy, University of Delaware, Newark, DE 19716-2570, USA*

^{||}*International Centre for Materials Science, Jawaharlal Nehru Centre for Advanced Scientific Research (JNCASR), Jakkur P.O., Bangalore 560064, India*

[⊥]*Department of Physics, Indian Institute of Science, Bangalore 560012, India*

[#]*School of Advanced Materials, Jawaharlal Nehru Centre for Advanced Scientific Research (JNCASR), Jakkur P.O., Bangalore 560064, India*

**E-mail: kanishka@jncasr.ac.in (K.B.); goutam@iisermohali.ac.in (G.S.)*

Methods

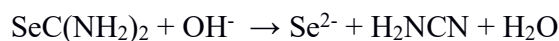
Reagents. Bismuth nitrate ($\text{Bi}(\text{NO}_3)_3 \cdot 5\text{H}_2\text{O}$, Alfa Aesar, 99.9%), selenourea ($\text{SeC}(\text{NH}_2)_2$, Alfa Aesar, 99.9%), potassium hydroxide (KOH, S D Fine-Chem Limited (SDFCL)), sodium hydroxide (NaOH, SDFCL), Disodium EDTA ($\text{C}_{10}\text{H}_{14}\text{O}_8\text{Na}_2\text{N}_2 \cdot \text{H}_2\text{O}$, SDFCL) and ethanol were used without any further purification.

Synthesis procedure. 100 mg (0.206 mmol) of $\text{Bi}(\text{NO}_3)_3 \cdot 5\text{H}_2\text{O}$, 12.7 mg (0.103 mmol) of $\text{SeC}(\text{NH}_2)_2$ and 306.8 mg (0.824 mmol) of disodium EDTA were sequentially added at a 5 minutes interval into 20 ml water in a glass beaker. The solution was stirred continuously. The addition of $\text{Bi}(\text{NO}_3)_3 \cdot 5\text{H}_2\text{O}$ into water results in a milky white color solution which turns into an orange color solution after the addition of $\text{SeC}(\text{NH}_2)_2$. The solution becomes clear after the addition of disodium EDTA. Finally, 120 mg (2.14 mmol) of KOH and 320 mg (8 mmol) of NaOH were added into the solution which turns the solution color black. After 10 minutes of stirring, the solution was put to rest which results in precipitation of the dark brown color nanosheets. We observed that nanosheets of similar morphology and thickness can also be obtained without using disodium EDTA, however, in that case, the required amount of water solvent is much higher, 200 ml. These were then washed with alcohol and water and centrifuged to remove disodium EDTA. The purified product was then dried in a vacuum oven at 150 °C.

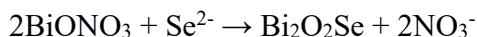
Step I: In water, $\text{Bi}(\text{NO}_3)_3$ undergoes hydrolysis to produce BiONO_3 and the process of hydrolysis is expedited in alkaline medium:



Step II: Selenourea $\text{SeC}(\text{NH}_2)_2$ undergoes decomposition in alkaline medium to generate selenide ions (Se^{2-}) along with cyanamide (H_2NCN):



Step III: In the final step, Se^{2-} interacts with BiONO_3 to form $\text{Bi}_2\text{O}_2\text{Se}$ which is precipitated as dark brown color product in the aqueous medium.



X-ray diffraction (XRD). Powder XRD patterns were collected in a Panalytical diffractometer with $\text{Cu K}\alpha$ radiation ($\lambda = 1.5406 \text{ \AA}$) at room temperature. XRD data of the as synthesized nanosheets were collected after dispersing the nanosheets in ethanol and drop casting on to a glass slide.

Band gap measurement. Diffuse reflectance spectroscopy was carried out using a Perkin Elmer Lambda 900, UV/VIS/NIR spectrometer from which absorption data was calculated using Kubelka-Munk equation: $\alpha/S = (1 - R)^2/2R$ where α , S and R are the absorption coefficient, scattering coefficient and reflectance, respectively. The optical band gap was then determined from the energy variation of α/S .

X-ray photoelectron spectroscopy (XPS). XPS measurement was carried out using an Omicron nanotechnology spectrometer with an $\text{Mg-K}\alpha$ (1253.6 eV) x-ray source.

Field emission scanning electron microscopy (FESEM). FESEM imaging was carried out using a FEI NOVA NANO SEM 600 with operating energy of 15 kV. Energy dispersive spectroscopy (EDX) analysis was carried out with an attached EDX genesis instrument.

Transmission electron microscopy (TEM). TEM studies were carried out using a FEI TECNAI G² 20 STWIN TEM operated at 200 keV and an aberration corrected FEI TITAN3 operating at 300 keV. EDX compositional analysis and elemental mapping were carried in STEM imaging mode. Very dilute solution of $\text{Bi}_2\text{O}_2\text{Se}$ nanosheets dispersed in ethanol was drop casted on holey carbon coated Cu grid and used for the TEM studies.

Inductively coupled plasma atomic emission spectroscopy (ICP-AES). ICP-AES was carried out for compositional analysis in a Perkin-Elmer Optima 7000DV instrument. For ICP-AES study, powdered nanosheets were dissolved in aqua regia ($\text{HNO}_3:\text{HCL} = 3:1$) and then this solution was further diluted using Millipore water.

Atomic force microscopy (AFM). Bruker Innova microscope in tapping mode was used to carry out AFM studies using an antimony doped silicon tip.

Raman Spectra. Room temperature Raman spectra of $\text{Bi}_2\text{O}_2\text{Se}$ bulk and nanosheet samples were collected on a Horiba Jobin Yvon LabRAM HR800 spectrometer using a He-Ne laser (632.8 nm).

Differential Scanning Calorimetry (DSC): A METTLER-TOLEDO differential scanning calorimeter (DSC 822 e) was used to collect DSC data with a ramp rate of 1 K/min in N_2 atmosphere.

Piezoresponse force microscopy (PFM). The measurements were done using an Asylum research AFM (MFP-3D) with an additional high voltage amplifier. The sample was mounted on a conducting sample holder which was directly connected to the ground of the amplifier. The conductive AFM cantilever having a Pt-Ir tip on it was brought in contact with the sample (nanosheets). An AC excitation of 4V riding on a dc bias voltage (V_{dc}) was applied between the tip and the amplifier ground. The response of the sample to the electrical stimulus was detected through the reflection of the laser beam from the end of the cantilever onto a position sensitive photo diode. In order to ensure that the hysteretic effects are due to ferroelectricity which may otherwise arise from electrostatic and electrochemical effect, all the measurements were performed following SS-PFM (switching spectroscopy piezoresponse force microscopy) initiated by Jesse et al.^{1,2} In this method, instead of sweeping V_{dc} continuously, bias is applied in sequence of pulses where the phase and amplitude measurements are done in the “off” states and an appreciable

change is observed in the “off-state” results as compared to the “on-state” measurements which is a clear evidence of the minimization of electrostatic effects. We further performed the topographic imaging after the spectroscopic measurements, where no topographic modification was observed which usually occurs due to the electrochemical reaction between the tip and sample.

Dielectric measurements. For dielectric measurements, Bi₂O₂Se nanosheets were pressed into a pellet. Dielectric properties were then measured in the temperature range from room temperature to 573 K and in the frequency range 200 Hz to 1 MHz with an ac excitation of 20 mV using a Solartron 1296A impedance analyzer.

Density functional theory (DFT) calculations. The first principles electronic structure calculations are performed within the framework of density functional theory (DFT) using generalized gradient approximation (GGA) of the Perdew-Burke-Ernzerhof (PBE)³ form for the exchange-correlation functional as implemented in the Vinea Ab-initio Simulation Package (VASP).⁴ The projector augmented wave (PAW)⁵ pseudo-potentials are used to describe the core electrons. Electronic wave-functions are expanded using plane waves up to a cut-off energy of 600 eV. Periodic boundary conditions are employed and at least of 15 Å slab is used on the surface of few layers to eliminate the interaction between consecutive periodic images. The Monkhorst-Pack k -mesh is set to 11×11 ($11 \times 11 \times 4$) in the Brillouin zone for the self-consistent calculation of few layer cases (bulk), and all atoms are relaxed in each optimization cycle until atomic forces on each atom are smaller than 0.01 eV/Å. As it is well-known that GGA functional underestimates the band gap, all the band structures are computed by using hybrid Heyd-Scuseria-Ernzerhof (HSE06)⁶ functional and the GGA-relaxed crystal structure. It should be noted here that we did not include any effect of exciton binding energy in our DFT calculations to estimate the optical band gap. Biaxial strain is simulated by changing the lattice constant a , whereas the space group

I4/mmm is fixed. The symmetric structure represents the equilibrium positions of the atoms at a given strain value. The distorted structure is obtained by diagonally displacing both the Bi and the Se atoms, but in opposite directions from their equilibrium positions. In what follows, if \mathbf{R}_{Bi} , and \mathbf{R}_{Se} are the equilibrium planer positions of the Bi and Se atoms respectively in a symmetric structure, then in the distorted structure, they assume positions at $\mathbf{R}_{\text{Bi}} + \boldsymbol{\delta}$, and $\mathbf{R}_{\text{Se}} - \boldsymbol{\delta}$, respectively. The outermost Se layers are passivated with hydrogen atoms in order to balance the non-stoichiometry due to the additional Se layer.

Table S1. Elemental compositions as obtained from EDX analysis.

Element	Wt %	At %
O	6.18	40.8
Bi	79.66	40.26
Se	14.16	18.94
Total	100	100

Table S2. Elemental compositions as obtained from ICP-AES measurement.

Element	Wt %	At %
Bi	139.5 mg/lit	66
Se	23.81 mg/lit	31

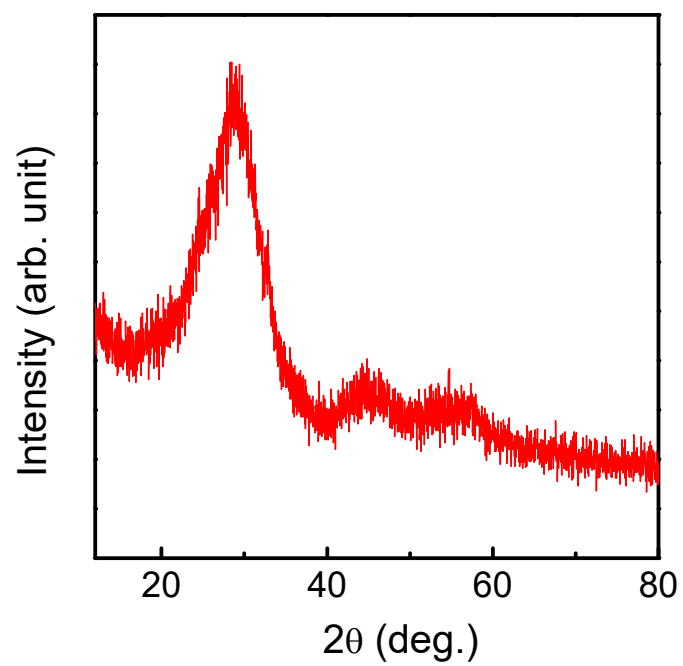


Figure S1. Room temperature XRD pattern of the as synthesized $\text{Bi}_2\text{O}_2\text{Se}$ nanosheets.

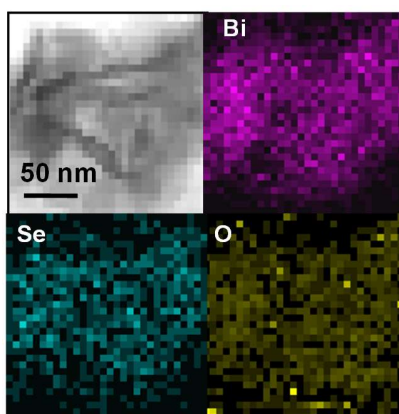


Figure S2. Elemental color mapping exhibiting a homogeneous distribution of Bi, O and Se in the Bi₂O₂Se nanosheet.

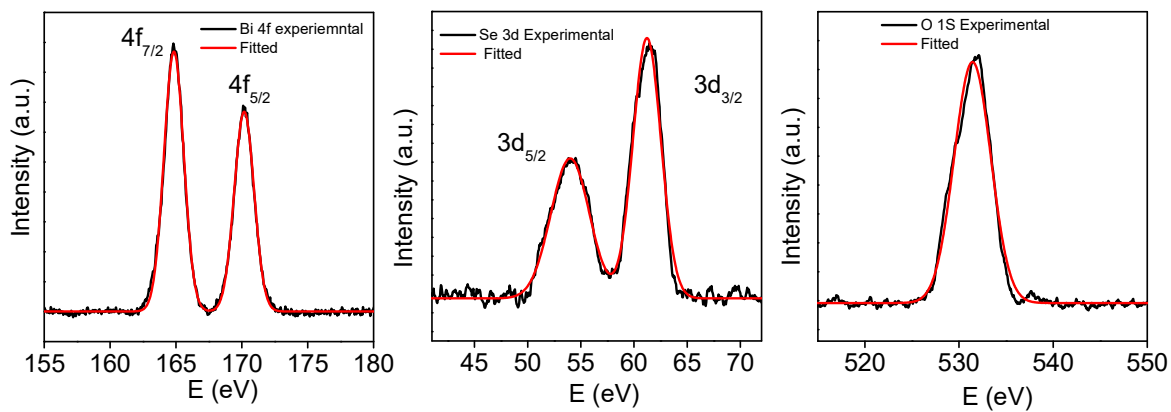


Figure S3. X-ray photoelectron spectra of $\text{Bi}_2\text{O}_2\text{Se}$ nanosheet showing the Bi 4f, Se 3d and O 1s peaks.

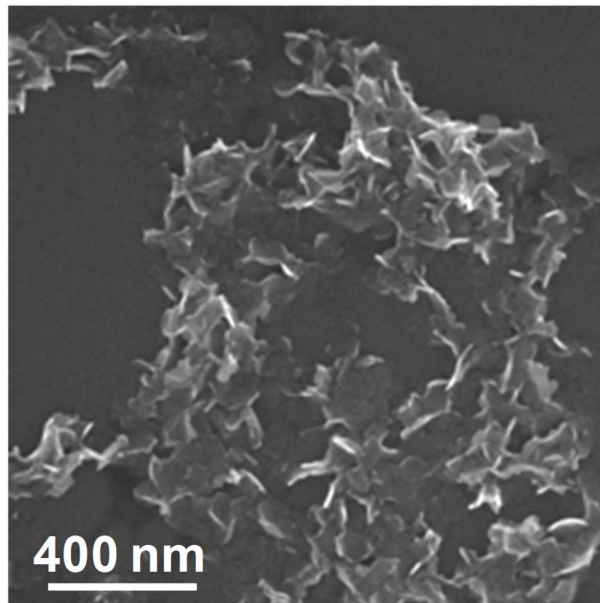


Figure S4. FESEM image of the Bi₂O₂Se nanosheets confirming the sheet like morphology.

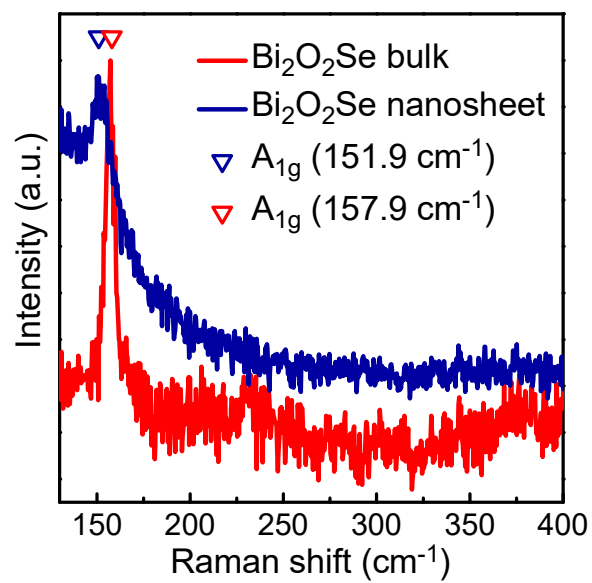


Figure S5. Room temperature Raman spectra of Bi₂O₂Se bulk and nanosheet.

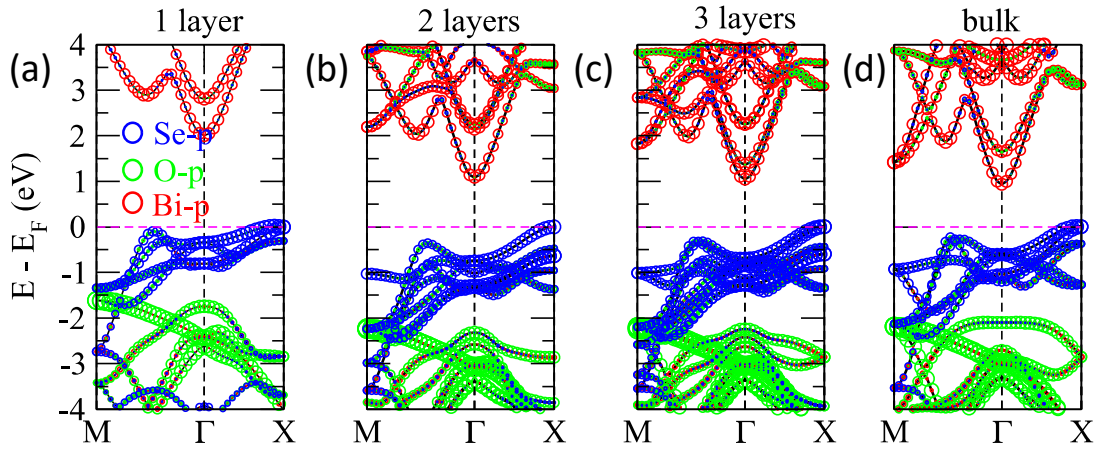


Figure S6. Thickness-dependent and orbital-decomposed band structure of (a) monolayer, (b) bilayer, (c) trilayer and (d) bulk $\text{Bi}_2\text{O}_2\text{Se}$, respectively. Red, green and blue circles indicate the fat-band structure, respectively, for Bi-p, O-p and Se-p orbitals. Magenta dashed line indicates the Fermi level.

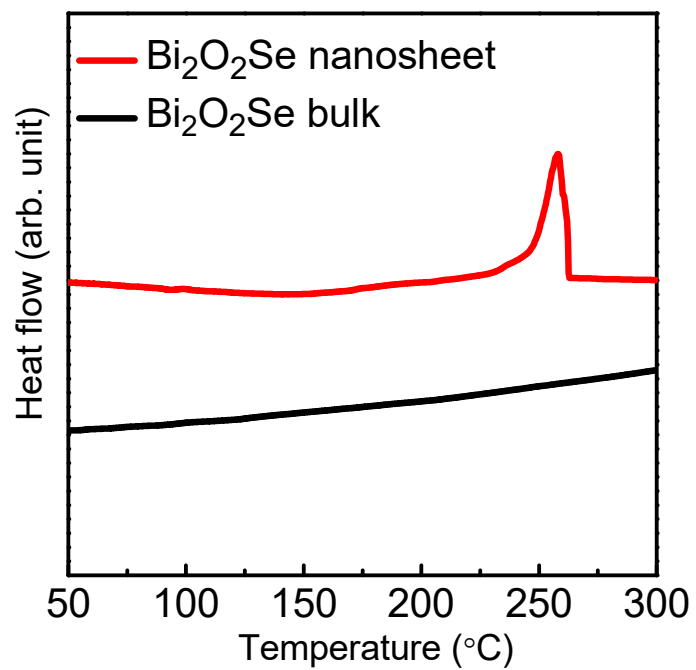


Figure S7. DSC signal of Bi₂O₂Se bulk and nanosheet samples. While the nanosheet sample shows the transition, the bulk does not.

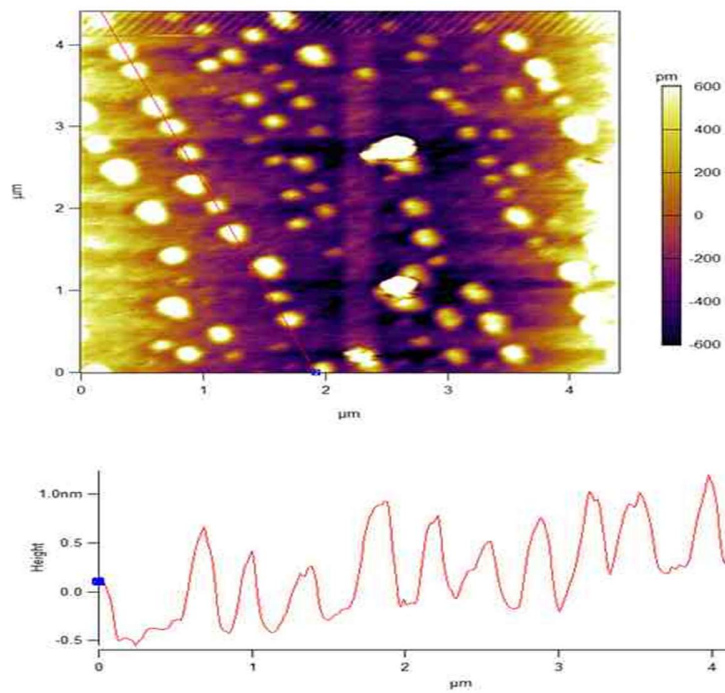


Figure S8. Topography showing 4.5 μm x 4.5 μm area used for PFM measurement.

References

1. Jesse, S.; Baddorf, A. P.; Kalinin, S. V. Switching spectroscopy piezoresponse force microscopy of ferroelectric materials. *Appl. Phys. Lett.* **2006**, *88*, 062908.
2. Jesse, S.; Mirman, B.; Kalinin, S. V. Resonance enhancement in piezoresponse force microscopy: Mapping electromechanical activity, contact stiffness, and Q factor. *Appl. Phys. Lett.* **2006**, *89*, 022906.
3. Perdew, J. P.; Burke, K.; Ernzerhof, M. Generalized Gradient Approximation Made Simple. *Phys. Rev. Lett.* **1996**, *77*, 3865–3868.
4. Kresse, G.; Furthmüller, J. Efficient iterative schemes for *ab initio* total-energy calculations using a plane-wave basis set. *Phys. Rev. B* **1996**, *54*, 11169–11186.
5. Kresse, G.; Joubert, D. From ultrasoft pseudopotentials to the projector augmented-wave method. *Phys. Rev. B* **1999**, *59*, 1758–1775.
6. Heyd, J.; Scuseria, G. E.; Ernzerhof, M. Hybrid functionals based on a screened Coulomb potential. *J. Chem. Phys.* **2003**, *118*, 8207–8215.